In situ observation of synthesized nanoparticles in ultra-dilute aerosols via X-ray scattering

McKibbin, Sarah R.; Yngman, Sofie; Balmes, Olivier; Meuller, Bengt O.; Tagerud, Simon; Messing, Maria E.; Portale, Giuseppe; Sztucki, Michael; Deppert, Knut; Samuelson, Lars

Published in:
Nano Research

DOI:
10.1007/s12274-018-2170-1

Publication date:
2019

Nano Research
2019, 12(1): 25–31

ISSN 1998-0124 CN 11-5974/O4
https://doi.org/10.1007/s12274-018-2170-1

Research Article

In situ observation of synthesized nanoparticles in ultra-dilute aerosols via X-ray scattering

Sarah R. McKibbin[1] (✉), Sofie Yngman[1], Olivier Balmes[2], Bengt O. Meuller[1], Simon Tågerud[1], Maria E. Messing[1], Giuseppe Portale[3], Michael Sztucki[4], Knut Deppert[1], Lars Samuelson[1], Martin H. Magnusson[1], Edvin Lundgren[1], and Anders Mikkelsen[1] (✉)

[1] *Department of Physics and Nanolund, Lund University, Box 118, 22100 Lund, Sweden*
[2] *MaxIV Laboratory, Lund University, Box 118, 22100 Lund, Sweden*
[3] *University of Groningen, Zernike Institute for Advanced Materials, Nijenborgh 4, NL-9747 AG Groningen, The Netherlands*
[4] *ESRF – The European Synchrotron, CS 40220, 38043 Grenoble Cedex 9, France*

Received: 23 March 2018 / **Revised:** 4 August 2018 / **Accepted:** 7 August 2018

ABSTRACT

In-air epitaxy of nanostructures (Aerotaxy) has recently emerged as a viable route for fast, large-scale production. In this study, we use small-angle X-ray scattering to perform direct in-flight characterizations of the first step of this process, i.e., the engineered formation of Au and Pt aerosol nanoparticles by spark generation in a flow of N_2 gas. This represents a particular challenge for characterization because the particle density can be extremely low in controlled production. The particles produced are examined during production at operational pressures close to atmospheric conditions and exhibit a lognormal size distribution ranging from 5–100 nm. The Au and Pt particle production and detection are compared. We observe and characterize the nanoparticles at different stages of synthesis and extract the corresponding dominant physical properties, including the average particle diameter and sphericity, as influenced by particle sintering and the presence of aggregates. We observe highly sorted and sintered spherical Au nanoparticles at ultra-dilute concentrations ($< 5 \times 10^5$ particles/cm^3) corresponding to a volume fraction below 3×10^{-10}, which is orders of magnitude below that of previously measured aerosols. We independently confirm an average particle radius of 25 nm via Guinier and Kratky plot analysis. Our study indicates that with high-intensity synchrotron beams and careful consideration of background removal, size and shape information can be obtained for extremely low particle concentrations with industrially relevant narrow size distributions.

KEYWORDS

aerosol, nanoparticle synthesis, *in situ* analysis, small-angle X-ray scattering, Aerotaxy

1 Introduction

Aerosol nanoparticles are the subject of inquiry for a broad range of topics, including the global rise of soot production, applications in smart coatings, and as catalytic seeding agents [1–4]. The presence of particles as an atmospheric contaminant has been of particular concern for respiratory health, which has fueled investigations into combustion byproducts and flame-synthesized aerosols. A particularly useful tool has been high-intensity synchrotron sources and free-electron lasers, which even allow for *in situ* studies of dilute samples and the reconstruction of single soot-particle structures in-flight [5–7]. Owing to the substantial development of high-pressure experiments and the increasing beam intensity of synchrotron facilities, it is becoming possible to investigate samples close to real atmospheric pressures and under *in situ* industrial conditions [8, 9]. While nanoparticles can be characterized by collecting a high density of particles after production or observing processes on particles supported by an underlying substrate or composite material [10, 11], results obtained in such a way may be influenced by additional inter-particle or particle–substrate interactions. Thus, *in situ* techniques to reveal the true nature of dilute aerosol systems are crucial for studying the particle size, distributions, and surface chemistry.

Well-controlled synthesis methods of aerosol nanoparticles for industrial applications are in need of analytic techniques to investigate the particles without extraction from the production environment and exposure to ambient conditions [12]. However, it is challenging to observe the low density of particles that result from strictly controlled synthesis processes, as this often involves particle sorting. There are a substantial number of previous reports on aerosol flame-produced particles [13–18] and nanoparticle fabrication in-solution [19–21]. However, these cases have rather high particle concentrations compared with the present case. There are few *in situ* investigations on aerosol nanoparticles using other synthesis methods. In this work, we demonstrate small-angle X-ray scattering (SAXS) using high-brilliance synchrotron radiation as a means to observe and characterize metallic particles, which are controllably synthesized via spark generation, in a gas flow. Aerosol Au particles similarly synthesized in a controlled way (either via spark generation or thermal evaporation) have recently been used as seeding agents for III-V nanowires (NWs) in a novel technique termed "Aerotaxy" [3], which, by eliminating the need for a supporting substrate during growth, has economic potential for nanostructured photovoltaics and optoelectronic devices [22–24]. In this process, large volumes of GaAs NWs with tuneable crystal structures are

Address correspondence to Sarah R. McKibbin, sarah.mckibbin@ftf.lth.se; Anders Mikkelsen, anders.mikkelsen@sljus.lu.se

continuously grown from Au nanoparticles in a flow reactor containing a carrier gas (N or He) at ambient pressures. The development of *in situ* accessible characterization techniques to observe such growth processes during production under realistic industrial conditions will not only improve the understanding of precursor adsorption and nucleation mechanisms on a fundamental level but also allow for broader application of such novel technologies. Since Au provides a large X-ray scattering cross-section, such metallic aerosol nanoparticles are an ideal proof-of-principle material system to study manufactured gas-based particulates *in situ*.

In this study, we use SAXS to perform *in situ* ensemble-averaged structural characterization of Au and Pt nanoparticles in a N_2 gas flow during particle production via spark generation. By detecting diffracted and scattered light through this dilute system, we can perform structural characterization of the particles at various stages of synthesis to determine the size and shape distributions and obtain information on the inter-particle interactions. We demonstrate the ability to characterize the nano-aerosol at normal operating pressures of spark-generated nanoparticle synthesis in the gas flow, which presents considerable new experimental challenges and requires careful data treatment. Specifically, we measure extremely low particle concentrations, which are substantially lower than previously reported values for aerosols and in-solution, thereby pushing the detection limits of small-angle scattering performed with high-brilliance synchrotron X-ray light.

2 Experimental

2.1 Aerosol nanoparticle synthesis, characterization, and experimental setup

Metallic nanoparticles were supplied from the output of a portable in-house built aerosol spark generator. A full description of the operation and output of this system is provided elsewhere [25, 26]. The major components of the aerosol generator of interest for this work were a spark chamber containing exchangeable electrodes; a sintering furnace, which heated and melted the particles into spherical distributions (with a material-dependent temperature range that is typically 600–1,200 °C); and a differential mobility analyzer (DMA) used for size selection of the particles. During our experiment, we examined Au sintering at 600 °C and Pt sintering at 1,150 °C. In a deposition chamber, an electrostatic precipitator was utilized to focus the charged particles onto the collector electrode via electrostatic deposition. These components are shown in the schematic of Fig. 1. In the spark chamber, a plasma channel was formed between electrodes when a high voltage was applied, and as the breakdown voltage was reached, high-energy sparks caused local heating and rapid evaporation of the source electrodes, producing particles in the carrier gas. For standard operation of the spark generator, the flow of N_2 through the system was set at 1.68 L/min, with a slight overpressure of 1,015 mbar. The variable spark conditions were 30–50 mA and 12 kV, with an electrode separation of 2–3 mm, and were tuned to maximize the particle output.

2.2 SAXS experiment and data analysis

In situ measurements were performed such that the output of the aerosol particle generator containing a flow of particles in N_2 was redirected through an X-ray analysis flow cell at various stages of production (as schematically illustrated in Fig. 1(b)). The analysis cell contained removable thin polyimide windows (Kapton, DuPont) for frequent replacement in the case of particle deposition.

While the high voltage (HV) was on and a high particle count was observed on the electrometer, a measurement was taken. After turning off the HV for spark generation but leaving the flow of N_2 gas and other functions the same as for operation, we waited until

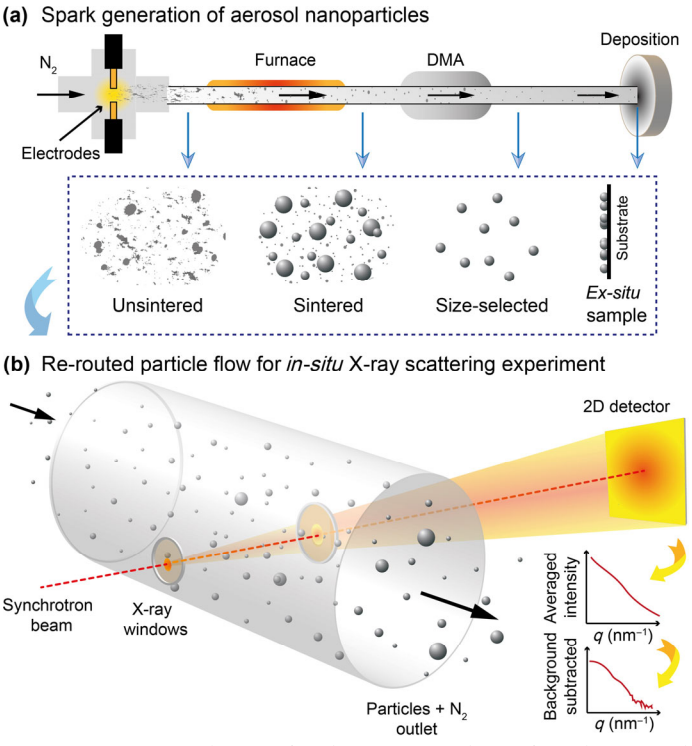

Figure 1 Experimental setup for the *in situ* analysis of spark-generated nanoparticles. (a) Nanoparticles are produced via spark generation from source electrodes and flow through various components (e.g., a high-temperature furnace for reshaping and DMAs for diameter filtering) to engineer the output. The particles can then be electrostatically deposited onto a substrate for *ex situ* post-production analysis. (b) Alternatively, the produced aerosol of the nanoparticles and carrier gas is re-routed at different points of production for *in situ* X-ray analysis. Light scattered through this X-ray flow cell is collected on a 2D detector, which is radially averaged to produce a one-dimensional (1D) plot of the normalized scattered light intensity vs. the scattering wave vector $\boldsymbol{q}$. After background subtraction, the structural information of our dilute aerosol system is revealed.

the electrometer particle count decreased to zero before taking the background measurements. This ensured that any signal from pre-existing or in-measurement deposited particles on the windows of the X-ray chamber were negated after background subtraction. By shining an X-ray light at the aerosol flow at different stages of production, we studied the particles in both their un-sintered and sintered states. For most of the *in situ* results shown in Figs. 3 and 4, we bypassed both DMAs and observed the full distribution of produced particles. For the results shown in Fig. 5, we utilized one DMA after particle sintering to select particles of a particular radius.

SAXS measurements were performed at the European Synchrotron Radiation Facility (ESRF) at both the ID02 time-resolved ultra-small-angle scattering beamline [27] and the BM26 DUBBLE SAXS/wide-angle X-ray scattering (WAXS) beamline [28, 29]. A Rayonix MX-170HS detector (with an active area of 170 mm × 170 mm) was used at the ID02 beamline. A Pilatus 1M detector (with an active area of 169 mm × 179 mm) was used for SAXS, and a 300K-W linear Pilatus detector was used for WAXS at the DUBBLE beamline. The beam had an energy of 12.25 keV (1.012 Å) with a diameter of ~ 500 μm for BM26 and an energy of 12.46 keV (0.99 Å) with an area of 100 μm × 200 μm for ID02.

At ID02, the recorded two-dimensional (2D) images were corrected for detector artifacts and normalized to absolute units using standard beamline procedures based on secondary standard intensity calibrants. Further data reduction was performed using the SAXS utilities software [30]. The normalized scattered intensity was plotted as a function of the scattering wave vector $\boldsymbol{q}$. The scattering vector is defined as $\boldsymbol{q} = (4\pi/\lambda)\sin\theta$, where 2θ is the scattering angle, and λ is

the X-ray wavelength. Owing to the high dilution of the particles, the resulting scattering intensity curves are essentially the Fourier transform of the particle form factor [31]. The particle geometry can be determined either via fitting with shape-dependent model functions or by using shape-independent approaches. We utilized both methods to estimate features related to the particle distribution, average radius of gyration, geometric radius, agglomerate size, and dimensionality of the agglomerates.

Simulation and best fit of the scattering intensity in Fig. 3 was achieved using the SASfit software.

3 Results and discussion

To put the results of the direct *in situ* experiment on particles in a gas in context, we first consider the expected output of the aerosol generator. Once particles are produced in the gas flow in the high-voltage spark chamber, they are passed through a charging device containing a radioactive ^{63}Ni film to provide them with a known electric-charge distribution (in this case, a Boltzmann distribution is utilized). This allows for later accurate sorting based on electrical mobility in the DMAs and an estimated live particle count during particle production from an electrometer. The electrometer measures the current of particles flowing into a Faraday cup filter, which is related to the particle charge. In this way, spark generation of particles generally produces an output with a lognormal size distribution with diameters of 1–100 nm, although the precise output is affected by several parameters, including the electrode separation, applied current and voltage, and gas flow in the system [26]. Using the measured concentrations of size-selected particles, their charge distribution, and the transfer function of the DMA setup, the real distribution of particles before size selection can be calculated via matrix inversion [32].

Two recorded size distributions of un-sintered and sintered Au particles produced by the aerosol spark generator are shown in Fig. 2(a). For un-sintered particles, the total integrated particle count is 9.3×10^7 particles/cm^3, and for sintered particles, it is 8.0×10^7 particles/cm^3. Some particle losses are expected for the sintered aerosol owing to particle coarsening and the accumulation of particles on the internal walls of the furnace and the tubing of the generator.

Previously, it has been possible to study samples with low volume fractions using SAXS of 10^{-6} [5, 17, 33] and even down to 10^{-8} [18], as demonstrated by observing combustion byproducts. We can use a spherical approximation to estimate the total volume fractions of the aerosols we have studied. Because the sintered particles themselves are nearly spherical, the estimate for these particles are more accurate than the un-sintered case; however, we can place an upper bound on the maximum possible volume fraction of the un-sintered particles. The distributions in Fig. 2 thus provide volume-fraction estimates of 1×10^{-9} and 7×10^{-10} for the un-sintered and sintered particles, respectively, which are at least an order of magnitude lower than previously measured values.

As a reference for in-flight measurements, we initially performed *ex situ* SAXS analysis of Au particles on pre-prepared polyimide film substrates (Kapton DuPont) to correlate these results with *in situ* experiments. However, the process of removing the particles from the production environment and depositing them on a substrate may affect the subsequent analytical characterizations. Spherical Au particles size-selected for 60-nm mobility diameters were deposited on Kapton substrates with different deposition times to produce three samples with densities of 200, 25, and 0.2 particles/μm^2 (the sample densities were calibrated via scanning electron microscopy (SEM) imaging, as shown in section S1 in the Electronic Supplementary Material (ESM)). In this case, size selection was achieved by first selecting un-sintered aggregates with a mobility diameter of 60 nm and then, after sintering, performing a second stage of filtering to select 60-nm-diameter particles, which led to a very accurate size distribution.

At the DUBBLE beamline of the ESRF, we performed a combination of SAXS and WAXS on these samples. The WAXS signal (shown in Fig. S1(d) in the ESM) for the highest-density sample (200/μm^2) confirmed the crystallinity, but these measurements were not possible for the lower-density samples. Figure 2(b) presents the SAXS curves measured for these static Au particles on Kapton samples. In the high-q region, all samples exhibited q^{-4} intensity decay, which is typical for spherical particles with a homogeneous electron density [31, 34]. The two higher-density samples exhibited a good signal-to-noise ratio and weak oscillations, indicating a relatively low polydispersity with a particle radius of 27–30 nm, based on the minima positions of the spherical form factor, confirming the conditions used by the DMA filters. However, because particles are deposited on top of each other, there is vastly more inter-particle and particle–substrate interaction, which may lead to particle deformation. The lowest-density sample should also contain spherical particles of well-defined radii, but the high noise level and low structural clarity make interpretation difficult. This highlights the need for an in-aerosol analysis method, particularly for samples of low concentrations.

We can consider the low-density sample as a test case for the resolution limit for the SAXS experiments and to anticipate the signal quality for the *in situ* experiments. Using an approximate beam diameter of 500 μm and 0.2 particles/μm^2, approximately 4×10^4 particles are sampled for this static sample. The estimated total mass is then 9×10^{-11} g for particles 30 nm in radius (Au density of 19.3 g/cm^3). From the spark-generator distributions shown in Fig. 2(a), we can also calculate the total mass of 4×10^{-8} g/cm^3 for the

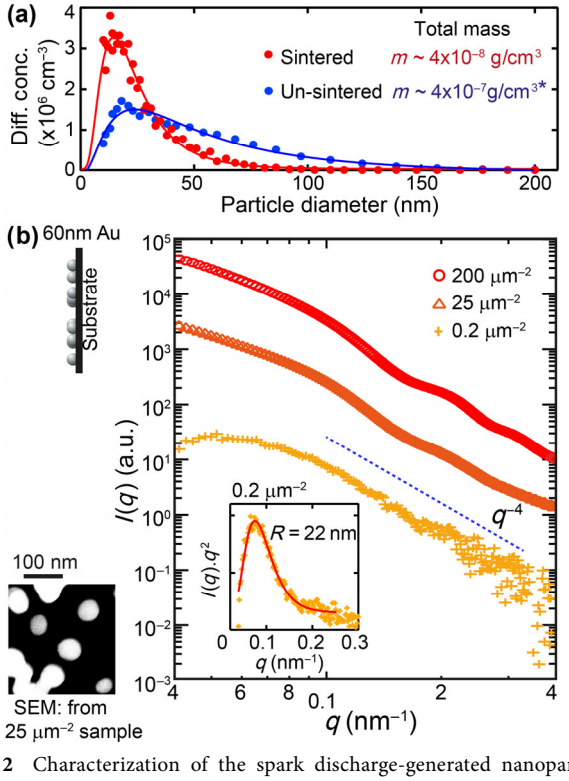

Figure 2 Characterization of the spark discharge-generated nanoparticles. (a) Calculated differential concentrations and size distributions of spark-generated un-sintered (blue) and sintered (red) Au nanoparticles. (b) *Ex situ* SAXS results for the three deposited Au samples, showing the 1D scatter plot intensity I as a function of the scattering vector $\boldsymbol{q}$ and (plot inset) the Kratky plot of $I(q)\cdot q^2$ vs. q for the lowest-density Au sample (the calculated average aerodynamic volume of un-sintered particles is 10 times larger than that after sintering owing to the compact-sphere approximation). The SEM inset shows the 25-μm^{-2} case.

unfiltered Au particles for the sintered flow. Assuming marginal losses, the un-sintered particles have a calculated mass of 4×10^{-7} g/cm^3. This suggests a larger average aerodynamic diameter for the un-sintered particles, which arises from the use of a compact-sphere approximation. In reality, only ~ 10% of the calculated mass is Au (because the agglomerates consist of non-spherical chains of clustered aggregates). Therefore, the total maximum sampled mass for the *in situ* experiments ranges approximately from 10^{-9} g (un-sintered) to 10^{-11} g (sintered), for a flow-chamber diameter of 1–2.5 cm (for experiments conducted at ID02 and BM26). Thus, we can expect to observe a similar degree of scattering (and signal-to-noise ratio) for the unfiltered *in situ* experiments as for the lowest-concentration size-selected static sample, which highlights the challenges in extracting reliable information on the particles at such low concentrations.

Ordinarily, a simple analysis can be performed by presenting the data in a Guinier plot ($\ln[I(q)]$ as a function of q^2), where a linear fit of the low-q region can be used for estimating the nanoparticle size. Specifically, the radius of gyration R_g is calculated using the equation slope = $R_g^2/3$ [34]. However, we have insufficient data points for $q <$ 0.03 where this holds true ($R_g \cdot q < 1$).

Instead, we focus on Kratky analysis, which considers $I(q) \cdot q^2$ vs. q. The Kratky plot for the low-density (0.2 particles/μm^2) sample is shown in the inset of Fig. 2(b). By fitting a lognormal distribution to this data, we can calculate the gyration radius R_g of 23 nm from the observed peak maximum $R_g = \sqrt{3} / q_{max}$ [34], where q_{max} was located at 0.075 nm^{-1}. This corresponds to a geometric radius r of 30 nm from $R_g = \sqrt{\frac{3}{5}} r$ [34], which is in excellent agreement with the targeted size selection performed by the DMAs.

We now consider *in situ* measurements. Operating the nanoparticle generator at the DUBBLE beamline, we re-routed the flow of particles in the system to go through our X-ray flow cell for the first *in situ* analysis. For this experiment, the sample environment-to-detector distance was fixed at 6.1 m, and we used two 25-μm-thick Kapton film windows on a 2.5-cm-wide cylindrical flow cell. By changing the source electrodes in the spark chamber, we produced and were able to detect via SAXS both Au (the seeding agent for GaAs Aerotaxy NWs) and Pt nanoparticles, as shown in Figs. 3(a) and 3(b), respectively, in a flow of N_2, in both their un-sintered and sintered (post-melt) states. Here, to maximize the density of particles in the flow, we did not utilize particle filtering for size selection. The two types of particles exhibited similar results, but the signal-to-noise ratio for the Au particles was slightly better, possibly owing to the larger scattering cross-section for Au [35].

Typical SAXS traces for the Au particles are shown in Fig. 3(a) (blue triangles and red circles for un-sintered and sintered particles, respectively) together with the best fit to the data (black lines). The Kratky plots are shown in Figs. 3(c) and 3(d), which provided estimates of 30 and 22 nm for the radius of gyration for Au and Pt, respectively (corresponding to geometric radii of 38 and 28 nm, respectively). However, the high degree of polydispersity and weak nature of the scattering did not allow this method to be used for the un-sintered particles. Nonetheless, from the best-fit line obtained using the SASfitting software, we could determine mass-fractal aggregation with an average radius of 5.4 nm for the un-sintered particles and large polydispersity of 40% with an average radius of 22 nm for the sintered Au particles (5–100 nm). Similar results were obtained for the unfiltered Pt particles shown in Fig. 3(b), with the SASfitting procedure yielding radii of 5 and 16 nm for the un-sintered and sintered particles, respectively.

These results confirm the expected spark-generated metallic particle outputs observed previously via *ex situ* transmission electron

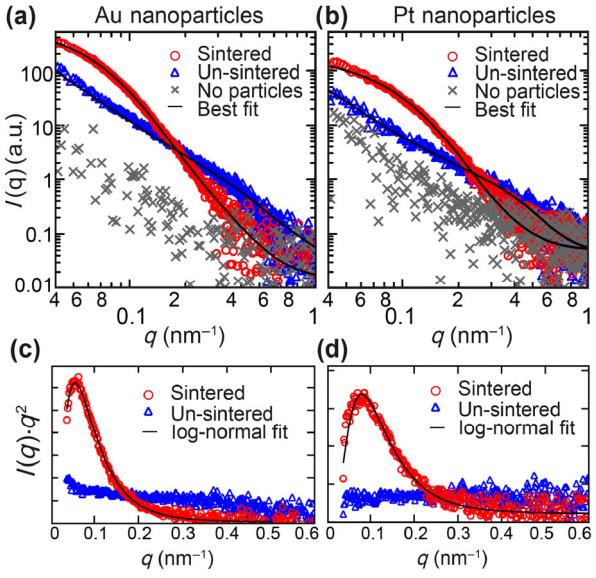

Figure 3 *In situ* SAXS measurements of spark-generated Au and Pt particles. (a) Au particles before (blue triangles) and after (red circles) particle melting in a sintering furnace. (b) Pt particles in un-sintered (blue) and sintered (red) states. When the particle production in the gas flow was halted, the signal was reduced to immeasurable noise levels, confirming that no particles were present (gray crosses). Fits to the data are shown in black. (c) and (d) Kratky plots for Au and Pt particles, respectively, along with lognormal fits to the sintered particles.

microscopy (TEM) analysis and detailed DMA surveying [25, 26, 36–39] (TEM images of polydisperse spark-generated Au particles are included in section S2 in the ESM). The data also indicate the well-understood sintering mechanisms for aerosols—both the coagulation phase for un-sintered particles, where small primary particles initially collide in the gas flow and cluster together into complex agglomerate chains [40], and the sintering process, where agglomerates consisting of several small particles melt into spherical particles with a larger minimum diameter [25] (TEM images showing Au particles with and without sintering are included in section S2 in the ESM, to illustrate the main structural differences between these un-sintered agglomerates and the reshaped Au particles).

Furthermore, we observed that the signal immediately returned to the background level after the spark production of Au particles ceased (shown by the gray "×" symbols in Figs. 3(a) and 3(b)), eliminating the possibility that the increase in the signal intensities originated from particle build-up on the X-ray windows; rather, they are true *in situ* characterizations. The signal for the spark-off measurement for Pt particles did not decrease as abruptly, suggesting that there was some degree of collection of the Pt particles on the flow-cell windows.

We used a larger flow cell than is often used for gas-phase experiments, which was necessary to maintain a laminar flow in the cell. The use of smaller flow cells or setups containing smaller internal outlets within a larger flow cell led to substantial turbulence of the aerosol. This allowed significant particle build-up on the X-ray windows, which then dominated and completely obscured any signal due to the particles in the gas flow.

We then performed investigations at the high-resolution SAXS beamline ID02 of the ESRF to investigate the resolution limit for *in situ* studies on aerosol nanoparticles. After the aerosol undergoes size selection, we are left with a small fraction of the material from the unfiltered flow, such that the already extremely dilute aerosol with low volume fractions of 10^{-9}–10^{-10} is reduced by another order of magnitude. A sample-to-detector distance of 15 m was used, and a 1-cm-wide four-way flow cell was devised such that the 200-μm-wide mica film windows were laterally separated from the laminar flow in order to reduce the particle build-up on the windows.

This large sample-to-detector distance provided us with more data in the low-q region, which was important for performing accurate particle-size analysis.

Figure 4 presents the scattering results for unfiltered Au particles in their un-sintered (blue diamonds) and sintered states (red circles) in the gas flow. We observe behavior similar to that shown in Fig. 3 but with improvement of the signal-to-noise ratio, which was partly due to the higher brilliance of ID02 compared with BM26. This is also offset by the fact the maximum electrometer counts for the particle densities were measuring approximately only 50% of the particle output of the previous experiments at BM26. However, there is a downturn at the lowest q values, which arises as an artifact from the background subtraction, limiting the usable data in this region. For this reason, the Kratky plot analysis should be considered as more reliable in our case than the Guinier plot analysis, although both are presented here for comparison between the sintered and un-sintered particles. The un-sintered particles exhibit characteristics similar to those for SAXS on folded long-chain proteins without a linear Guinier region (Fig. 4(b)), but an estimate of the average nanoparticle dimension (R_g = 12 nm) is obtained from the Kratky plot in Fig. 4(c). These factors again indicate the mass-fractal agglomeration of the un-sintered particles.

We clearly observe that the sintered particles follow the q^{-4} relation expected for spherical particles. The analysis based on the Guinier plot shown in Fig. 4(b) suggests an estimated dimension of R_g = 19 nm. Similarly, the Kratky plot in Fig. 4(c) gives approximations of R_g = 19 nm and r = 25 nm, with a lognormal distribution typical for spherical particles (although the noise level becomes high above q = 0.3 nm^{-1}).

These results are within the expected range of values for unfiltered particles. Although some of the values are higher than the previous values obtained in Fig. 3, the precise size distribution of the particles produced by the spark generator can vary between experimental runs.

For these *in situ* experiments, it is critical to consider the background subtraction for each measurement for ensuring that any contribution from particle collection on the windows is negated. To confirm that these results are predominantly a result of the *in situ* gas-phase particles, we investigated the unfiltered sintered Au particles in the gas flow through the flow chamber but removed the windows for measurement. Thus, we obtained an open chamber similar to those used in other aerosol experiments on soot particles produced through combustion [5]. These results are presented in Fig. 5, and we confirmed the previous results (when Kapton windows were in place on the flow cell) that indicated well-defined spherical particles with a Kratky R_g = 19 nm in Fig. 5(b), corresponding to r = 25 nm (with an additional coarse estimation of R_g = 18 nm from the inset showing the Guinier plot in Fig. 5(a)). For this measurement, a sample-to-detector distance of only 4 m was used.

Standard operation of the generator requires continuous pumping through the system, such that all aerosol products are collected and passed through a nano-filter before going to an exhaust. To prevent particle loss to the hutch environment, we maintained the pumping power but reduced the system pressure in the system to 975 mbar, which is slightly below atmospheric pressure, ensuring the collection of aerosol products by the exhaust. This technique may allow a small degree of particle oxidation due to the mixing of atmospheric O_2 with the N_2 carrier gas (although the likelihood of this occurring with Au particles is minimal) and the dilution of the particle concentration in the gas flow.

We then investigated whether we could detect and characterize particles with a selected radius via SAXS. This represents the most controlled engineering of nanoparticles in a gas flow for *in situ* analysis but is also the most challenging for detection. Size selection

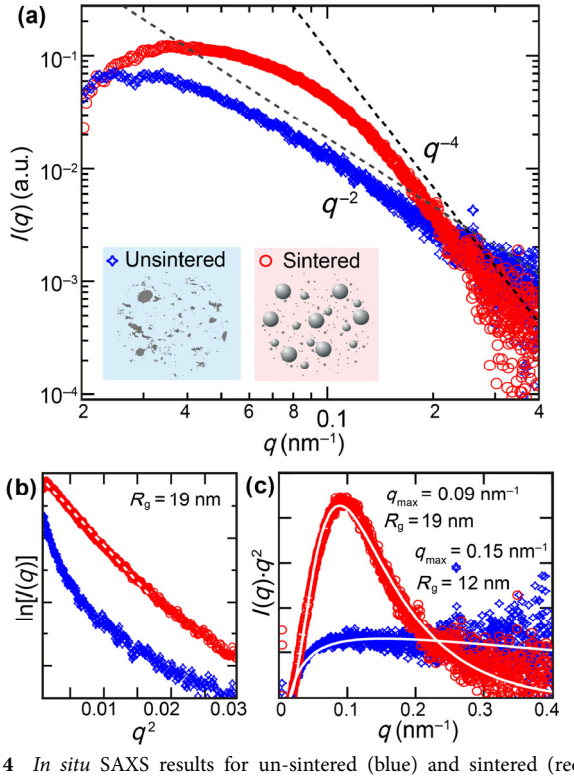

Figure 4 *In situ* SAXS results for un-sintered (blue) and sintered (red) Au aerosol nanoparticles. (a) Scatter plot where the sintered particles exhibit a q^{-4} relation, (b) Guinier plot ln(I) vs. q^2, indicating an average radius of 19 nm for the sintered particles and the presence of agglomerates for un-sintered particles given by nonlinearity. (c) Kratky plots of $I(q)\cdot q^2$ vs. q, showing an average R_g of 19 nm with some polydispersity for sintered particles and R_g = 12 nm with unfolded behavior for un-sintered particles, which is indicative of long-chain agglomerates.

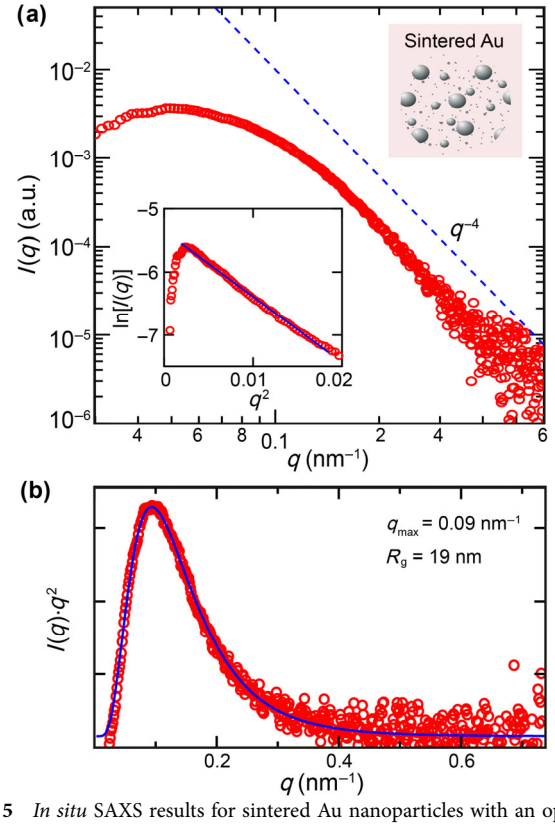

Figure 5 *In situ* SAXS results for sintered Au nanoparticles with an open cell. (a) 1D scatter plot, (inset) Guinier plot of ln(I) vs. q^2 indicating R_g = 18 nm. (b) Kratky plot $I(q)\cdot q^2$ vs. q showing R_g = 19 nm and r = 25 nm, as well as a clear lognormal relation indicating spherical particles.

is performed by a DMA, where an electric field between the flow chamber walls and a charged internal rod electrode allow for sorting based on the electrical mobility diameter [41]. Two DMAs are utilized under normal operation of the spark generator: the first before particle sintering and the second after for a more accurate selection and narrow distribution of produced particles [37]. However, because we already pushed the boundary of the detection limit for SAXS, we only utilized the second DMA (after sintering) for size selection, to avoid unnecessary particle losses.

Figure 6 presents *in situ* scattering results for sintered Au particles in a flow of N_2, which underwent size selection for a mobility diameter of 50 nm. Considering the calculated particle distribution from Fig. 2(a), the total volume fraction for these filtered particles is on the order of 4×10^{-11}–1×10^{-10}, which is two to three orders of magnitude lower than that of aerosols measured previously via SAXS. We observe that despite the elevated noise level in the scattering signal compared with the previous measurement due to the extremely low density of particles in the gas flow, a spherical relationship $I \propto q^{-4}$ can be detected in the high-q region (fitting 0.9 $nm^{-1} < q < 0.25$ nm^{-1} gives $\propto q^{-4.1}$). However, owing to the quality of the data for $q > 0.2$ nm^{-1} we cannot determine whether the asymmetry is a real feature of the data due to polydispersity or an artifact resulting from the background subtraction. A linear fit to a limited q range, as shown in the inset of Fig. 6(a), can be used to estimate the particle radius: $R_g = 22$ nm. Similarly, fitting a lognormal to the Kratky representation of the data in Fig. 6(b) gives a $q_{max} = 0.07$ nm^{-1}, which corresponds to $R_g = 25$ nm (for $q < 0.2$ nm^{-1}) and a geometric radius of 32 nm. Given the low signal-to-noise ratio, we indicate by the dotted lines a range of possible q_{max} values giving upper and lower bounds to the gyration radius $R_g = 19$–29 nm. This corresponds to a geometric radius of $r = 25$–37 nm. Therefore, despite the weak nature of the signal and our use of only one DMA (which limits the accuracy of size selection filtering) we confirm an engineered radius of approximately 25 nm for the Au nanoparticles.

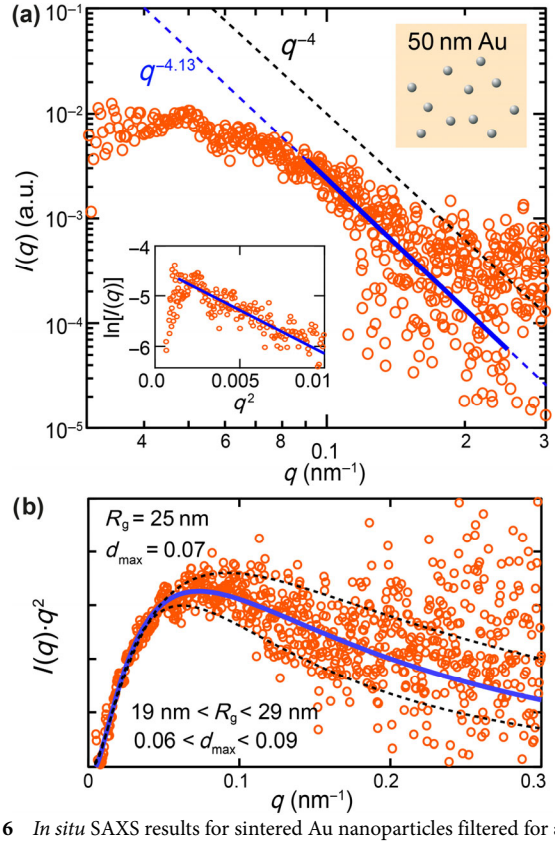

Figure 6 *In situ* SAXS results for sintered Au nanoparticles filtered for a 25-nm radius. (a) 1D scatter plot showing that the line of best fit between $q = 0.09$ and 0.25 nm^{-1}, yielding $I \propto q^{-4.1}$. A linear fit to the Guinier plot (ln(I) vs. q^2) gives R_g = 22 nm (inset). A lognormal fit to the Kratky plot ($I(q)\cdot q^2$ vs. q) in (b) suggests R_g = 25 nm and a geometric radius of $r = 32$ nm, in reasonable agreement with the conditions chosen for particle filtering.

For our system, it is not easy to observe the signal contribution arising from particles in the gas without performing background subtraction to negate the effects of scattering through the cell windows or the air flow in the chamber and beamline environment. In some cases, the choice of background used for subtraction can have a significant effect on the shape of the resulting curve, i.e., those taken directly prior to or directly after flowing Au particles through the system. This likely arises from the comparable particle collection on windows compared with the particles in the gas flow or fluctuations in the carrier gas, meaning that there were insufficient aerosol particles for detection. We included the raw untreated data from Fig. 6 in section S3 in the ESM (Fig. S4) to illustrate the importance of background subtraction.

For the *in situ* results presented in this work (Figs. 3–6), we only presented data where the particles in the cell dominated the signal and the choice of background (before and after flowing particles through the cell) did not affect the resulting curve.

Thus, we emphasize that extreme care must be taken with reference measurements and the background choice when performing analysis of other such extremely dilute systems. Concern for such issues may increase in the future owing to the ever-expanding interest in nanoscale structures and single-particle characterization techniques. However, as indicated by our results in Fig. 6, we were able to extract the physical characteristics of these well-synthesized particles in the flow at volume fractions as low as 10^{-11}, which is several orders of magnitude lower than what has been previously studied. This is of interest to the growing community working with engineered aerosol nanoparticles, particularly because it was not necessary to interfere with the aerosol output in any way that could increase the interaction between the particles in the flow or otherwise modify their properties.

4 Conclusions

We successfully studied for the first time an extremely dilute nanoaerosol within a commercially equivalent production environment, using high-brilliance synchrotron radiation. SAXS from spark-generated aerosol nanoparticles was analyzed at different stages of synthesis, within the carrier gas without extraction from the production environment. We were thus able to determine the presence of Au and Pt particle aggregation, the degree of sphericity of primary particles after sintering, and the average mobility diameters, which were all in agreement with previous *ex situ* studies. Furthermore, we were able to characterize extremely low concentrations of particles with volume concentrations several orders of magnitude below what has been previously possible for *in situ* studies, both for unfiltered distributions of particles and for particles having undergone controlled size selection to produce narrow size distributions.

We thus probed and revealed the limits of small-angle scattering detection, which is significant for all dilute systems—not just those examined in this study. These experiments present a critical step for future *in situ* experiments to observe and build a better understanding of the growth mechanisms for Aerosol NWs. Such a technique can also be used as a direct means to determine the reactive surface area of synthesized aerosol nanoparticles under different production conditions and would therefore be of interest to industries beyond semiconductor physics, such as catalysis and medical science.

Acknowledgements

This work was performed within Nanolund at Lund University, and was supported by the Knut and Alice Wallenberg Foundation, the Swedish Research Council (VR) and the Swedish Foundation for

Strategic Research (SSF). The Dutch Organization for Scientific Research (NWO) and the ESRF are acknowledged for providing beamtime for this project.

Electronic Supplementary Material: Supplementary material (containing additional SEM, TEM and XRD analysis of samples containing spark generated Au nanoparticles and details of necessary background subtraction for analysis of *in-situ* SAXS results) is available in the online version of this article at https://doi.org/10.1007/s12274-018-2170-1.

References

[1] Buseck, P. R.; Adachi, K. Nanoparticles in the atmosphere. *Elements* **2008**, *4*, 389–394.

[2] Strobel, R.; Pratsinis, S. E. Flame aerosol synthesis of smart nanostructured materials. *J. Mater. Chem.* **2007**, ***17***, 4743–4756.

[3] Heurlin, M.; Magnusson, M. H.; Lindgren, D.; Ek, M.; Wallenberg, L. R.; Deppert, K.; Samuelson, L. Continuous gas-phase synthesis of nanowires with tunable properties. *Nature* **2012**, *492*, 90–94.

[4] Magnusson, M. H.; Ohlsson, B. J.; Björk, M. T.; Dick, K. A.; Borgström, M. T.; Deppert, K.; Samuelson, L. Semiconductor nanostructures enabled by aerosol technology. *Front. Phys.* **2014**, *9*, 398–418.

[5] Beaucage, G.; Kammler, H. K.; Mueller, R.; Strobel, R.; Agashe, N.; Pratsinis, S. E.; Narayanan, T. Probing the dynamics of nanoparticle growth in a flame using synchrotron radiation. *Nat. Mater.* **2004**, *3*, 370–374.

[6] Zhang, R. Y.; Khalizov, A. F.; Pagels, J.; Zhang, D.; Xue, H. X.; McMurry, P. H. Variability in morphology, hygroscopicity, and optical properties of soot aerosols during atmospheric processing. *Proc. Natl. Acad. Sci. USA* **2008**, *105*, 10291–10296.

[7] Loh, N. D.; Hampton, C. Y.; Martin, A. V.; Starodub, D.; Sierra, R. G.; Barty, A.; Aquila, A.; Schulz, J.; Lomb, L.; Steinbrener, J. et al. Fractal morphology, imaging and mass spectrometry of single aerosol particles in flight. *Nature* **2012**, *486*, 513–517.

[8] Schnadt, J.; Knudsen, J.; Andersen, J. N.; Siegbahn, H.; Pietzsch, A.; Hennies, F.; Johansson, N.; Mårtensson, N.; Öhrwall, G.; Bahr, S. et al. The new ambient-pressure X-ray photoelectron spectroscopy instrument at MAX-lab. *J. Synchrotron Radiat.* **2012**, *19*, 701–704.

[9] Liu, X. S.; Yang, W. L.; Liu, Z. Recent progress on synchrotron-based *in-situ* soft X-ray spectroscopy for energy materials. *Adv. Mater.* **2014**, *26*, 7710–7729.

[10] Ingham, B. X-ray scattering characterisation of nanoparticles. *Crystallogr. Rev.* **2015**, *21*, 229–303.

[11] Wysocka, I.; Kowalska, E.; Trzciński, K.; Łapiński, M.; Nowaczyk, G.; Zielińska-Jurek, A. UV-vis-induced degradation of phenol over magnetic photocatalysts modified with Pt, Pd, Cu and Au nanoparticles. *Nanomaterials* **2018**, *8*, 28.

[12] Lu, Y. F.; Fan, H. Y.; Stump, A.; Ward, T. L.; Rieker, T.; Brinker, C. J. Aerosol-assisted self-assembly of mesostructured spherical nanoparticles *Nature* **1999**, *398*, 223–226.

[13] Our, F. X.; Parent, P.; Laffon, C.; Marhaba, I.; Ferry, D.; Marcillaud, B.; Antonsson, E.; Benkoula, S.; Liu, X. J.; Nicolas, C. et al. First in-flight synchrotron X-ray absorption and photoemission study of carbon soot nanoparticles. *Sci. Rep.* **2016**, *6*, 36495.

[14] Ferraro, G.; Fratini, E.; Rausa, R.; Fiaschi, P.; Baglioni, P. Multiscale characterization of some commercial carbon blacks and diesel engine soot. *Energy Fuels* **2016**, *30*, 9859–9866.

[15] Sztucki, M.; Narayanan, T.; Beaucage, G. *In situ* study of aggregation of soot particles in an acetylene flame by small-angle X-ray scattering. *J. Appl. Phys.* **2007**, *101*, 114304.

[16] Jerby, E.; Golts, A.; Shamir, Y.; Wonde, S.; Mitchell, J. B. A.; LeGarrec, J. L.; Narayanan, T.; Sztucki, M.; Ashkenazi, D.; Barkay, Z. et al. Nanoparticle plasma ejected directly from solid copper by localized microwaves. *Appl. Phys. Lett.* **2009**, *95*, 191501.

[17] Hammler, H. K.; Beaucage, G.; Kohls, D. J.; Agashe, N.; Ilavsky, J. Monitoring simultaneously the growth of nanoparticles and aggregates by *in situ* ultra-small-angle X-ray scattering. *J. Appl. Phys.* **2005**, *97*, 054309.

[18] Wang, J.; Seifert, S.; Winans, R. E.; Tolmachoff, E.; Xin, Y. X.; Chen, D. P.; Wang, H.; Anderson, S. L. *In situ* X-ray scattering and dynamical modeling of Pd catalyst nanoparticles formed in flames. *J. Phys. Chem. C* **2015**, *119*, 19073–19082.

[19] Letzel, A.; Gökce, B.; Wagener, P.; Ibrahimkutty, S.; Menzel, A.; Plech, A.; Barcikowski, S. Size quenching during laser synthesis of colloids happens already in the vapor phase of the cavitation bubble. *J. Phys. Chem. C* **2017**, *121*, 5356–5365.

[20] Megens, M.; van Kats, C. M.; Bösecke, P.; Vos, W. L. *In situ* characterization of colloidal spheres by synchrotron small-angle X-ray scattering. *Langmuir* **1997**, *13*, 6120–6129.

[21] Smith, M. C.; Gilbert, J. A.; Mawdsley, J. R.; Seifert, S.; Myers, D. J. *In situ* small-angle X-ray scattering observation of Pt catalyst particle growth during potential cycling. *J. Am. Chem. Soc.* **2008**, *130*, 8112–8113.

[22] Wallentin, J.; Anttu, N.; Asoli, D.; Huffman, M.; Aberg, I.; Magnusson, M. H.; Siefer, G.; Fuss-Kailuweit, P.; Dimroth, F.; Witzigmann, B. et al. InP nanowire array solar cells achieving 13.8% efficiency by exceeding the ray optics limit. *Science* **2013**, *339*, 1057–1060.

[23] Borgström, M. T.; Wallentin, J.; Heurlin, M.; Fält, S.; Wickert, P.; Leene, J.; Magnusson, M. H.; Deppert, K.; Samuelson, L. Nanowires with promise for photovoltaics. *IEEE J. Sel. Top. Quantum Electron.* **2011**, *17*, 1050–1061.

[24] Qian, F.; Gradečak, S.; Li, Y.; Wen, C. Y.; Lieber, C. M. Core/multishell nanowire heterostructures as multicolor, high-efficiency light-emitting diodes. *Nano Lett.* **2005**, *5*, 2287–2291.

[25] Messing, M. E.; Johansson, K. A.; Wallenberg, R.; Wallenberg, K. Generation of size-selected gold nanoparticles by spark discharge—For growth of epitaxial nanowires. *Gold Bull.* **2009**, *42*, 20–26.

[26] Meuller, B. O.; Messing, M. E.; Engberg, D. L. J.; Jansson, A. M.; Johansson, L. I. M.; Norlén, S. M.; Tureson, N.; Deppert, K. Review of spark discharge generators for production of nanoparticle aerosols. *Aerosol Sci. Technol.* **2012**, *46*, 1256–1270.

[27] Narayanan, T.; Diat, O.; Bösecke, P. SAXS and USAXS on the high brilliance beamline at the ESRF. *Nucl. Inst. Methods Phys. Res. A.* **2001**, *467–468*, 1005–1009.

[28] Barnes, J. D.; Bras, W. Temperature-dependent three-dimensional small-angle scattering in semicrystalline polymers. *J Appl. Crystallogr.* **2003**, *36*, 664–668.

[29] Portale, G.; Cavallo, D.; Alfonso, G. C.; Hermida-Merino, D.; van Drongelen, M.; Balzano, L.; Peters, G. W. M.; Goossens, J. G. P.; Bras W. Polymer crystallization studies under processing-relevant conditions at the SAXS/WAXS DUBBLE beamline at the ESRF. *J. Appl. Crystallogr.* **2013**, *46*, 1681–1689.

[30] Sztucki, M. *On-Line Processing and Analysis of SAXS Data* [Online]. http://www.saxsutilities.eu (accessed Mar 23, 2018).

[31] Guinier, A.; Fournet, G. *Small Angle Scattering of X-Rays*; John Wiley and Sons: New York, 1955.

[32] Hagen, D. E.; Alofs, D. J. Linear inversion method to obtain aerosol size distributions from measurements with a differential mobility analyzer. *Aerosol Sci. Technol.* **1983**, *2*, 465–475.

[33] Mitchell, J. B. A.; Courbe, J.; Florescu-Mitchell, A. I.; di Stasio, S.; Weiss, T. Demonstration of soot particle resizing in an ethylene flame by small angle X-ray scattering. *J. Appl. Phys.* **2006**, *100*, 124918.

[34] Glatter, O.; Kratky, O. *Small Angle X-Ray Scattering*; Academic Press: London, 1982.

[35] *X-Ray Data Booklet: Center for X-Ray Optics and Advanced Light Source*; Lawrence Berkeley National Laboratory, University of California: Berkeley, CA, USA, 1982.

[36] Messing, M. E.; Svensson, C. R.; Pagels, J.; Meuller, B. O.; Deppert, K.; Rissler, J. Gas-borne particles with tunable and highly controlled characteristics for nanotoxicology studies. *Nanotoxicology* **2012**, *7*, 1052–1063.

[37] Messing, M. E.; Westerström, R.; Meuller, B. O.; Blomberg, S.; Gustafson, J.; Andersen, J. N.; Lundgren, E.; van Rijn, R.; Balmes, O.; Bluhm, H. et al. Generation of Pd model catalyst nanoparticles by spark discharge. *J. Phys. Chem. C* **2010**, *114*, 9257–9263.

[38] Tabrizi, N. S.; Xu, Q.; van der Pers, N. M.; Lafont, U.; Schmidt-Ott, A. Synthesis of mixed metallic nanoparticles by spark discharge. *J. Nanopart. Res.* **2009**, *11*, 1209–1218.

[39] Tabrizi, N. S.; Xu, Q.; van der Pers, N. M.; Schmidt-Ott, A. Generation of mixed metallic nanoparticles from immiscible metals by spark discharge. *J. Nanopart. Res.* **2010**, *12*, 247–259.

[40] Schwyn, S.; Garwin, E.; Schmidt-Ott, A. Aerosol generation by spark discharge. *J. Aerosol Sci.* **1988**, *19*, 639–642

[41] Knutson. E. O.; Whitby, K. T. Aerosol classification by electric mobility: Apparatus, theory, and applications. *J. Aerosol Sci.* **1975**, *6*, 443–445.